POLITECNICO DI TORINO
Repository ISTITUZIONALE

Impact of Oxide Aperture Geometry on Noise Performance Degradation in 850 nm Multimode VCSELs for Datacom Applications

Original
Impact of Oxide Aperture Geometry on Noise Performance Degradation in 850 nm Multimode VCSELs for Datacom Applications / Rimoldi, C., Columbo, L.L., Tibaldi, A., Debernardi, P., García, S.R., Raabe, C., Gioannini, M.. - ELETTRONICO. - (2024). (24th International Conference on Transparent Optical Networks (ICTON) Bari (Ita) 14-18 July 2024) [10.1109/icton62926.2024.10647732].

Availability:
This version is available at: 11583/2994023 since: 2024-12-20T17:43:44Z

Publisher:
IEEE

Published
DOI:10.1109/icton62926.2024.10647732

Terms of use:

This article is made available under terms and conditions as specified in the corresponding bibliographic description in the repository

Publisher copyright
IEEE postprint/Author's Accepted Manuscript

©2024 IEEE. Personal use of this material is permitted. Permission from IEEE must be obtained for all other uses, in any current or future media, including reprinting/republishing this material for advertising or promotional purposes, creating new collecting works, for resale or lists, or reuse of any copyrighted component of this work in other works.

(Article begins on next page)

06 November 2026

Impact of Oxide Aperture Geometry on Noise Performance Degradation in 850 nm Multimode VCSELs for Datacom Applications

Cristina Rimoldi[1*], Lorenzo L. Columbo[1], A. Tibaldi[1], *Member, IEEE*, P. Debernardi[2], Sebastian Romero García[3], Christian Raabe[3], M. Gioannini[1], *Member, IEEE*

1. Dipartimento di Elettronica e Telecomunicazioni, Politecnico di Torino, Corso Duca degli Abruzzi 24, IT-10129, Torino, Italy

2. Consiglio Nazionale delle Ricerche (CNR-IEIIT), Corso Duca degli Abruzzi 24, IT-10129, Torino, Italy

3. Cisco Optical, Nordostpark 12, D-90411, Nuremberg, Germany

**e-mail: cristina.rimoldi@polito.it*

ABSTRACT

We study an 850 nm multimode VCSEL with an elliptical oxide aperture. The device is dynamically modeled through a time domain mode expansion approach, accounting for coherent mode coupling and spatial hole burning. Here, Relative Intensity Noise (RIN) spectra display spurious peaks, limiting the device performance. Analytical considerations and electromagnetic simulations allow us to identify good parametric regions for aperture geometry design, potentially improving the laser noise performance.

Keywords: multimode VCSELs, oxide aperture, frequency mixing, noise performance, relative intensity noise, high-speed data transmission.

1. INTRODUCTION

Multimode VCSELs have been progressively employed in the context of short-reach data transmission fiber links in data centers [1], due to their effective trade-off between bandwidth and achievable power. In this context, circular oxide aperture VCSELs present the drawback of emitting almost degenerate modes, distanced only by a few GHz, and often leading to beatings between modes mediated by spatial hole burning, resulting in unwanted peaks at low frequencies in the Relative Intensity Noise (RIN). Here, elliptical oxide aperture VCSELs [2] offer an attractive solution allowing to separate modal frequencies and consequently push their potential beatings beyond present-day receiver bandwidths. While this temporary solution has allowed an improvement of RIN performance, the lack of a deeper understanding of the physical origin beyond the formation of such peaks, hinders the adoption of more effective design solutions, capable to stand the test of time, when next-generation receivers with larger bandwidths will become available. In this contribution, we experimentally and numerically characterize an 850 nm multimode VCSEL with an elliptical oxide aperture, which has been effectively designed to suppress one polarization. Our time domain mode expansion approach [3] allows to limit the electric field dynamics to a few relevant transverse modes while also accounting for coherent mode coupling. Our simulations allow to address the laser modal power-current characteristics, the RIN spectrum, optical spectrum, and intensity modulation response. We demonstrate that the spurious peaks observed in the RIN, are the result of nontrivial four-wave mixing processes and suggest a few simple design rules to fabricate lasers with improved performance.

2. EXPERIMENTAL CHARACTERIZATION

The typical result of a near-field measurement of the VCSEL is displayed in Fig. 1(a). The measurement was performed by collecting light at the output of the VCSEL through a 20x objective lens to obtain a far-field collimated beam. The laser beam is then directed through a series of 4 consecutive 750 nm blazed reflective diffraction gratings, the role of which is spatially separating transverse modes at different wavelengths. Finally, in order to obtain the laser near-field profile, the gratings output is sent through a tube lens to a polarization-resolved compact camera. In Fig. 1(a), we can observe five Hermite-Gauss transverse modes C_m. In Fig. 1(b), we report the laser experimental optical spectrum at I_{bias}=4.5 mA, collected through a high-resolution optical spectrum analyzer (Yokogawa, AQ6370D), where we can identify the five lasing modes with the five main peaks at the frequencies $\nu_{1\text{-}5} \approx 0$, 194, 263, 413, 475 GHz, setting the frequency of C_1 as a reference. Finally, in Fig. 1(c), we show its corresponding RIN spectrum, acquired with a 40 GHz RIN measurement system (SYCATUS, A0010-040). Here, we can clearly observe the presence of three peaks, at the frequencies of 8.3, 18, and 27.3 GHz.

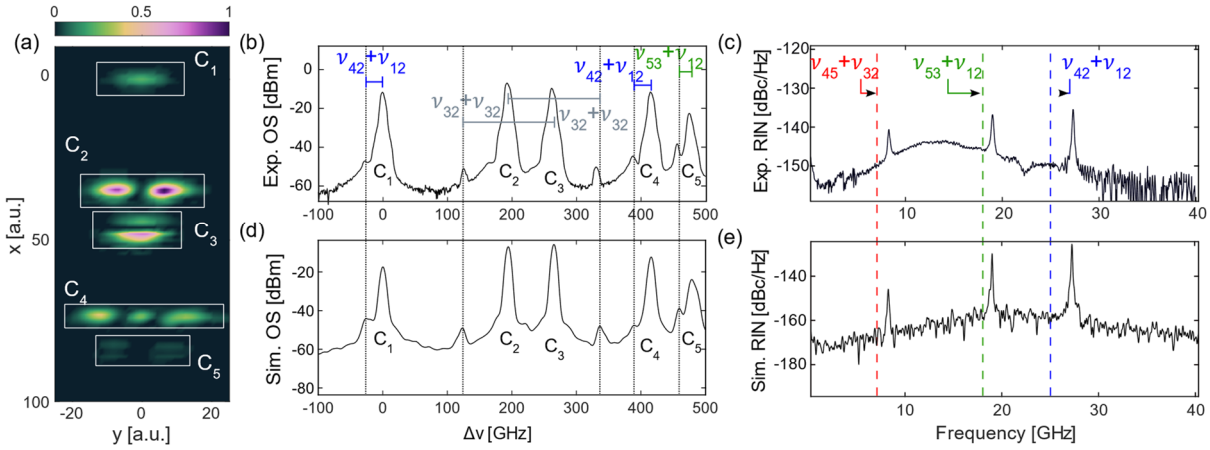


Figure 1. (a) Near-field measurement of an 850 nm multimode VCSEL with an elliptical oxide aperture. C_m identifies the Hermite-Gaussian modes, of which we see the spatial intensity profile. (b,d) Experimental (b) and simulated (d) optical spectrum with labeled emitting modes. (c,e) Experimental (c) and simulated (e) RIN. The vertical dashed lines in (c) identify the predicted beating frequencies. The bias current is I_{bias}=4.5 mA. Other labels are defined and discussed in the text.

3. MODELING AND RESULTS

We adopt a time-domain mode expansion approach, based on [4] and modify the model to include the contribution of carrier diffusion in the transverse plane. Input parameters in our simulator are the number and type of transverse modes relevant for the laser dynamics, the angular frequency detuning of each mode $\omega_m=2\pi\nu_m$ with respect to C_1, with angular frequency ω_0, as well as the modal photon lifetime $\tau_{p,m}$, which are tuned to match the threshold currents of the modes. These parameters are determined through experimental characterization of the device as well as with the support of electromagnetic simulations. The set of equations reads as follows [3]:

$$\frac{dE_m(t)}{dt} = \left[i\Delta\omega_m - \frac{1+i\alpha}{2\tau_{p,m}}\right] E_m(t) + \\ + \frac{\Gamma G_N}{2}(1+i\alpha)\int_0^\infty\int_0^{2\pi} \rho d\rho d\varphi \frac{E(\rho,\phi,t)}{1+\varepsilon N_p(\rho,\phi,t)} C_m^*(\rho,\phi)[N(\rho,\phi,t)-N_0] + S_{sp}(t) \qquad (1)$$

$$\frac{dN(\rho,\phi,t)}{dt} = \frac{\eta_i I(\rho,\phi,t)}{eV} - \frac{N(\rho,\phi,t)}{\tau_e} - \frac{n_g^2\epsilon_0 G_N}{2\hbar\omega_0}\frac{|E(\rho,\phi,t)|^2}{1+\varepsilon N_p(\rho,\phi,t)}[N(\rho,\phi,t)-N_0] + D\nabla_\perp^2 N(\rho,\phi,t), \qquad (2)$$

The introduced variables, functions of *(ρ,φ,t)* represent: the carrier density *N*, the current *I*, the (slowly varying) electric field *E*, and the photon density N_p. In particular, for the current $I(\rho,\phi,t)$ we consider a flat-top transverse profile, with dimensions approximating those of the VCSEL oxide aperture. $E_m(t)$ is the projection of the electric field *E(ρ,φ,t)* onto modes $C_m(\rho,\varphi)$, which are the Hermite Gaussian modes, as defined in [4],

$$E_m(t) = \int_0^\infty\int_0^{2\pi} \rho d\rho d\varphi\, E(\rho,\phi,t) C_m^*(\rho,\phi). \qquad (3)$$

The linewidth enhancement factor is α, $G_N=g_N v_g$ with g_N the differential gain and v_g the group velocity, ε is the gain compression factor, and $S_{sp}(t)$ is the spontaneous emission. In the carrier density equation, η_i is the current injection efficiency, τ_e is the carrier lifetime, *V* is the volume of the active region, n_g is the group refractive index, and ϵ_0 is the vacuum permittivity. Finally, $\nabla_\perp^2$ is the transverse Laplacian operator and *D* is the carrier diffusion coefficient. Our approach properly accounts for frequency mixing and coherent transverse mode coupling, which allows for a comprehensive and accurate description of the laser dynamics, differently from other models in literature. For an efficient numerical computation, it is preferable to scale the time variable in Eq. (1,2) as $\bar{t} = t/\tau_p$. Further, we set the following scalings [5]

$$\bar{E} = \sqrt{\frac{G_N\tau_e n_g^2\epsilon_0}{2\hbar\omega_0}}E;\ \bar{N} = (N-N_0)G_N\tau_p;\ \bar{I} = G_N\tau_p N_0\left(\frac{\eta_i I\tau_e}{eVN_0}-1\right). \qquad (3)$$

As a result, Eq. (1) and (2) become:

$$\frac{d\bar{E}_m(\bar{t})}{d\bar{t}} = \left[i\Delta\omega_m\tau_p - \frac{(1+i\alpha)\tau_p}{2\tau_{p,m}}\right]\bar{E}_m(\bar{t}) + \frac{1+i\alpha}{2}\int_0^\infty\int_0^{2\pi}\rho d\rho d\varphi \frac{\bar{E}(\rho,\phi,t)}{1+\varepsilon N_p(\rho,\phi,t)} C_m^*(\rho,\phi)\bar{N} + \tilde{S}_{sp}(\bar{t}) \qquad (4)$$

$$\frac{d\bar{N}(\rho,\phi,\bar{t})}{d\bar{t}} = \gamma\left[\bar{I}(\rho,\phi,\bar{t}) - \bar{N}\left(1+\frac{|\bar{E}(\rho,\phi,\bar{t})|^2}{1+\varepsilon N_p(\rho,\phi,\bar{t})}\right) + D\nabla_\perp^2\bar{N}(\rho,\phi,\bar{t})\right]. \qquad (5)$$

Where we have set $\gamma = \tau_p/\tau_e$ and rescaled the spontaneous emission term $\tilde{S}_{sp}(\bar{t})$ in order to account for the normalization on $E_m(t)$. The photon density N_p relates to the normalized electric field variable $\bar{E}$ as

$$N_p = \frac{|\bar{E}|^2}{G_N \tau_p} = \frac{n_g^2 \epsilon_0}{2\hbar\omega_0}|E|^2 \qquad (5)$$

Simulating the VCSEL behavior at I_{bias}=4.5 mA, we obtain the optical spectrum displayed in Fig. 1(d), where we can clearly identify the five lasing modes $C_{1\text{-}5}$. Further, in Fig. 1(e), we show the simulated RIN spectrum, where we can observe the presence of the same three peaks seen in the experiment. This demonstrates that our model is able to qualitatively simulate the laser RIN performance. The peaks in the spectral RIN can be analytically explained as follows. Starting from Eq. (1) and setting $\tilde{E}_m(t) = E_m(t)e^{-i\omega_m t}$, we obtain the following equation,

$$\frac{d\tilde{E}_m(t)}{dt} = -\frac{1+i\alpha}{2\tau_{p,m}}\tilde{E}_m(t) +$$
$$+\frac{\Gamma G_N}{2}(1+i\alpha)\, e^{-i\omega_m t}\int_0^\infty\int_0^{2\pi}\rho d\rho d\varphi \frac{E(\rho,\phi,t)}{1+\varepsilon N_p(\rho,\phi,t)} C_m^*(\rho,\phi)[N(\rho,\phi,t)-N_0] + \quad + S_{sp}(t)e^{-i\omega_m t} \qquad (6)$$

In the hypothesis, that carriers instantaneously follow the electric field, setting equal to zero the first order derivative in Eq. (2), we can derive an explicit relation between carrier density and electric field. Under this adiabatic approximation, neglecting diffusion and the gain compression factor and assuming weak field intensity ($|E|^2 \ll \frac{2\hbar\omega_0}{n_g^2\epsilon_0 G_N \tau_e}$), Eq. (6) can be reduced to

$$\frac{d\tilde{E}_m}{dt} = -\frac{1+i\alpha}{2\tau_{p,m}}\tilde{E}_m + \tilde{g}\Lambda\left(1-\gamma_{mmmm}\frac{|\tilde{E}_m|^2}{E_S^2} - 2\sum_{n\neq m}\gamma_{mmnn}\frac{|\tilde{E}_n|^2}{E_S^2}\right)\tilde{E}_m - \tilde{g}\Lambda\sum_{n,l,r*}\gamma_{mnlr}\frac{\tilde{E}_n\tilde{E}_l\tilde{E}_r^*}{E_S^2}e^{i(\omega_{nm}+\omega_{lr})t} \qquad (7)$$

With $\tilde{g} = \frac{\Gamma G_N(1+i\alpha)}{2}$, $E_S^2 = \frac{2\hbar\omega_0}{n_g^2\epsilon_0 G_N\tau_e}$, $\Lambda = \tau_e\left(\frac{\eta_i I}{eV} - \frac{N_0}{\tau_e}\right)$, and, most importantly,

$$\gamma_{mnlr} = \int_0^\infty\int_0^{2\pi}\rho d\rho d\varphi \;\; C_m^*\, C_n C_l\, C_r^* \qquad (8)$$

In Eq. (7) the first term on the RHS accounts for cavity loss and the frequency shift due to the carrier related α factor, while the second term accounts for stimulated emission. The third and fourth terms are the self-saturation and the cross-saturation induced on the *m*-th mode by the emergence of the *n*-th mode, respectively. Finally, the fifth term accounts for the four-wave mixing (FWM) process that causes oscillation of $\tilde{E}_m$ at frequency $\omega_{nm} + \omega_{lr} = \omega_n - \omega_m + \omega_l - \omega_r$. Note that the sum on n, l, r is intended to already exclude the cases for which $n - m + l - r = 0$. We highlight that, depending on the spatial overlap of transverse modes, the coefficients γ_{mnlr} can be null in some cases,. In the case of the considered elliptical VCSEL structure, the most relevant frequency beating conditions arising from the FWM term in Eq. (4), within a ≈40 GHz receiver bandwidth, are the following:

$$\nu_{45} + \nu_{32} = \nu_4 - \nu_5 + \nu_3 - \nu_2 \approx 7 \text{ GHz} \qquad (9)$$
$$\nu_{53} + \nu_{12} = \nu_5 - \nu_3 + \nu_1 - \nu_2 \approx 18 \text{ GHz} \qquad (10)$$
$$\nu_{42} + \nu_{12} = \nu_4 - \nu_2 + \nu_1 - \nu_2 \approx 25 \text{ GHz} \qquad (11)$$

The predicted frequencies are reported with vertical dashed lines in Fig. 1(c,e): here, we observe that Eqs. (9-11) identify the peaks in the experimental (and simulated) RIN. We assume that the slight discrepancy between predicted and observed values is simply due to the approximations adopted to obtain an analytical form for Eq. (4), while our full model (Eqs. (1-2)) perfectly reproduces the experimental RIN peak positions. Focusing now on the optical spectra, the frequency separations in Eq. (9-11) are supposed to be observed as sidebands of the modes involved in each FWM process. While sidebands of the beating frequency in Eq. (9), as well as a few others, cannot be observed due to the limited OSA resolution bandwidth, a sideband associated to Eq. (10) is present around mode C_5 (in green), and sidebands associated to Eq. (11) show up around mode C_1 and C_4 (in blue). Additionally, we also find two clear sidebands, highlighted in grey, which are also present in the experimental optical spectrum. These peaks are due to another FWM process with associated beating frequency $\nu_3 - \nu_2 + \nu_3 - \nu_2 \approx 138$ GHz, which cannot be observed through a RIN measurement due to the limited bandwidth of 40 GHz.

4. CONCLUSIONS

In conclusion, we propose an experimentally validated model that allows, through Eqs. (9-10), to give a guideline for elliptical VCSEL design on the most relevant FWM processes that can affect noise performance and, consequently, the transmission performance, when the VCSEL is employed for high-speed data transmission. Simulations with NRZ and PAM4 PRBS for applications in short-reach data transmission are currently ongoing.

ACKNOWLEDGEMENTS

This work was partially supported by the European Union under the Italian National Recovery and Resilience Plan (PNRR) of NextGenerationEU, partnership on "Telecommunications of the Future" (PE00000001 - program "RESTART"). CR acknowledges funding from research contract no. [32-I-13427-1] (DM 1062/2021) funded within the Programma Operativo Nazionale (PON) Ricerca e Innovazione of the Italian Ministry of University and Research.

REFERENCES

[1] V. Bhatt, et al., “Multimode Links Based on High-Speed VCSELs for Cost-Effective Data Center Connectivity”, Optical Fiber Communication Conference (OFC) 2024, paper Th1B.4.

[2] D. Gazula, et al. II-VI Delaware Inc, "VCSEL with elliptical aperture having reduced RIN", US20190341743A1, 2020.

[3] C. Rimoldi, et al., "Dynamical analysis of multimode VCSELs with elliptical oxide aperture," Proc. SPIE 12904, Vertical-Cavity Surface-Emitting Lasers XXVIII, 129040L (2024).

[4] F. Prati, et al., “Pattern formation in lasers”, Riv. Nuovo Cim., vol. 17, pp. 1-85 1994.

[5] L. Columbo, et al., “Self-mixing in multi-transverse mode semiconductor lasers: model and potential application to multi-parametric sensing,” Opt. Express vol. 20, pp. 6286-6305, 2012.